Negative piezoelectricity and enhanced electrical conductivity at the interfaces of two-dimensional dialkali oxide and chalcogenide monolayers

Anu Arora,* Ashima Rawat,* and Abir De Sarkar†
Institute of Nano Science and Technology, Sector 81, Manauli, Mohali, Punjab 140062, India

(Received 6 June 2022; revised 30 October 2022; accepted 23 January 2023; published 2 February 2023)

The negative piezoelectric coefficient in ferroelectric polymers has been widely studied. However, the same in the two-dimensional (2D) materials is scarcely reported, which stresses the need for its thorough investigation. Here, the 2D van der Waals (vdW) heterobilayers (vdWHs) of the dialkali metal monochalcogenide M_2X (M = Na, K, Rb, or Cs; and X = O, S, Se, or Te) monolayers show negative out-of-plane piezoelectricity. Out of all the explored heterobilayers of the family, the maximum piezoelectric strain coefficient in the out-of-plane direction $d_{33} = -39$ pm V^{-1} is found in the Na_2Te/Cs_2S system. This strong piezoelectric coefficient arises from the notable electrostatic potential energy difference and band offset between the constituent monolayers. The small out-of-plane Young's modulus ($Y \sim 11$ N m^{-1}), originating from the weak vdW interlayer bonding relative to the stronger intralayer bonding, accounts for the anomalous negative piezoelectricity in the heterostructure. The combination of minute out-of-plane ($Y =\sim 11$ N m^{-1}) and in-plane ($Y =\sim 23$ N m^{-1}) Young's moduli with small bending modulus (8.83 eV) and negative piezoelectric coefficient underlines the suitability of the proposed vdWH for stretchable and flexible piezotronic devices. Moreover, external perturbations are found to modify the properties of the system. The vertical compressive strain widens the band gap by elevating the conduction band minimum in the heterostructure. An externally applied electric field of low strength (-0.33 and $+0.31$ V/Å) is found to change the semiconducting heterostructure to metallic upon the closure of the band gap, which is attributed to the dropping of nearly free electron gas (NFEG) states to the Fermi level. A significant enhancement in electrical conductivity has been brought up by the NFEG states upon reaching the Fermi level, which inspires the use of the heterostructure in a nonresistive charge carrier transport application in electronics.

DOI: 10.1103/PhysRevB.107.085402

I. INTRODUCTION

With the discovery of the remarkable properties of graphene [1], two-dimensional (2D) materials have captured a plenty of attention [2] compared with the bulk materials. The emergence of several unique properties like enormous flexibility, high carrier conductivity, and piezoelectricity [3–6] at the nanoscale has encouraged the futuristic applications of 2D materials. Thus, 2D systems like transition metal dichalcogenides (TMDCs), trichalcogenides, and phosphorene [7–10] have been explored as semiconducting alternatives to pristine zero band gap graphene. While these pristine single layers exhibit different properties relative to their bulk counterparts, there is still ample scope for further improvement to reinforce their properties and enhance their potential in device applications. Consequently, scientific communities have been looking into possibilities to surmount the intrinsic limitations of monolayers and a synergistic combination of their unique properties. One of the avenues for maintaining structural integrity while retaining the critical features of monolayers lies in stacking individual monolayers vertically, forming van der Waals (vdW) heterobilayers [11–13]. The heterobilayers formed predominantly exhibit emergent properties due to interface effects, apart from the properties of the individual monolayers. Thus, ongoing research focuses on bringing up multifold improvements in 2D materials for their diverse applications in numerous fields [14,15].

The study of piezoelectric response in 2D systems has opened a wide window of opportunities for noncentrosymmetric monolayers in the sector of mechanical energy harvesting, where the ubiquitous mechanical energy in the surroundings can easily be renewed into useful electric energy. A 2D material having broken inversion symmetry, high flexibility, efficiency, and stability can be advantageously exploited for energy harvesting in low-powered devices, vibration-powered electronics, actuators, flexible or wearable devices, etc. Former investigations on monolayers like TMDCs ($d_{11} = 3$–9 pm V^{-1}) [16], boron binary and ternary V-group monolayers ($d_{11} = 0.5$–4.5 pm V^{-1}) [17], heterostructure MoS_2/WSe_2 [18], GaN/BP ($d_{33} = 40$ pm V^{-1}) [19], Janus transition metal ($d_{33} = 5$–12 pm V^{-1}), and Group-IV dichalcogenides [20,21] have revealed positive piezoelectric coefficients in the systems. However, the negative piezoelectric response in 2D systems is scantily detected. In this rarely found piezoelectric property, the material tends to show contraction along the applied electric field (EF) direction, bringing alternative electromechanical functionalities for the system in piezoelectric devices. In earlier studies on negative piezoelectricity in ferroelectric polymers like polyvinylidene difluoride (PVDF) [22] or vdW layered systems like $CuInP_2S_6$ (CIPS) [23] and bismuth tellurohalides [24], the weak vdW interaction among the interlayers has been

*These authors contributed equally this work.
†abir@inst.ac.in; abirdesarkar@gmail.com

held responsible for bringing out such an anomalous piezoelectric response in the system. Thus, the current research status warrants further investigation to uncover the possible source of anomalous negative piezoelectricity in 2D monolayers and vdW heterostructures to value additional piezoelectric properties for device applications.

Aside from the inherent features of monolayers, 2D systems respond very well to external stimuli, which can usher in intriguing qualities. Applying external perturbations is understood to be a practical method for improving the properties of 2D monolayers. A viable option for improving the characteristics of 2D monolayers can be comprehended by applying an external EF. The addition of the EF to the system is, in fact, found to bring considerable improvements in the pristine properties such as optical, thermal, adsorption, and band gap tunability of the system [25–28]. In very few materials, the nearly free electron gas (NFEG) states of the vacuum observed descending around the Fermi level through the vertical EF can be readily realized by gating in field-effect transistors [29–31]. These surface states are naturally unoccupied and are present at high energy levels near the vacuum. Moreover, as the NFEG states drop near the Fermi level, a significant boost in the catalytic activity, surface chemistry, and electrical conductivity can be expected through the availability of a large density of states (DOS) around the Fermi level. The latter is addressed in this paper, as it can significantly improve the performance of the device. Therefore, a comprehensive investigation of these states in 2D systems is crucial, as it obviates the need for resorting to the standard practices, such as doping, surface chemistry, and electrode design [32] for the purpose of enhancing or controlling electrical conductivity and catalytic activities. Moreover, it underscores the need to unveil the essential mechanism underlying the electric-field-induced shifting of NFEG states to near the Fermi level and its effects on electrical conductivity and catalytic activities.

In this paper, an insightful study on the 2D stable family of dialkali metal monochalogenide monolayers M_2X (M = Na, K, Rb, or Cs; and X = O, S, Se, or Te) and their van der Waal heterostructures has been systematically conducted. The intrinsic properties of monolayers, which include electronic, mechanical, and piezoelectric properties, have been theoretically investigated. The elastic properties revealed a high level of flexibility in the noncentrosymmetric M_2X monolayers, which motivated the exploration of their piezoelectric properties. Relative to the monolayers, the vdW heterostructures of the family showed an ample piezoelectric response. Colossal negative piezoelectricity in the Na_2Te/Cs_2S vdW heterostructure has been found. Thus, a detailed analysis of the peculiar negative piezoelectricity observed in the proposed 2D vdW heterostructure has been conducted for the purpose of unveiling its origin. Moreover, the external perturbations, for instance, external vertical strain and EF, are treated on the Na_2Te/Cs_2S heterostructure. Widening of the band gap is noticed with the compressive strain along the z direction. The gradual lowering and closure of the band gap by the normal EF, observed in this paper, is found to arise due to the shifting of NFEG states to the proximity of the Fermi level. The occurrence of NFEG states near the Fermi level influenced and boosted the electric conductivity in the heterostructure, which has been appropriately addressed in this paper. These findings can enable the application of the heterostructure in low-powered logic gate devices. In this paper, we aim to provide valuable insights into Na_2Te/Cs_2S heterostructure capabilities and thereby promote the designing of electromechanical, data storage, and enhanced electrical conductivities in devices built from the multifunctional vdW heterostructure.

II. COMPUTATIONAL DETAILS

First-principles density functional theory (DFT) implemented in the Vienna *Ab initio* Simulation Package (VASP) [33–36] is employed in this paper. The core electrons and exchange-correlation energy of the electrons are calculated using the projector augmented-wave potentials [37] and the Perdew, Burke, and Ernzerhof (PBE) generalized gradient approximation (GGA) [38,39]. The cutoff energy is set to be 500 eV for the plane-wave basis in the supercells and the convergence of total energy differences of two self-consistent cycles to be $< 10^{-4}$ eV. The atomic coordinates of the supercells are relaxed until the atomic forces reach < 0.01 eV/Å. The vacuum thickness > 20 Å is preferred to eliminate the periodic images along the z direction. With the inaccuracy in the PBE-optimized band gap calculation, hybrid functional calculations (HSE06) [40,41] are adopted to obtain more precise band gap and band edges for the systems. For the heterostructures, the vdW interactions are implemented by DFT-D3 proposed by Grimme *et al.* [42,43]. The Brillouin zone sampling is performed via the $18 \times 18 \times 1$ Γ-centered k-mesh for the supercells. The mixing parameter and the range separation parameter are set to 0.25 and 0.2 A^{-1}, respectively. The phonon dispersion is obtained on a $4 \times 4 \times 1$ supercell for the monolayers using PHONOPY code, built on the density functional perturbation theory (DFPT) method. The BOLTZTRAP2 package is utilized to investigate the electronic transport properties, which is based on the semiclassical Boltzmann transport equation within the constant relaxation time approximation [44]. A linear dipole correction is employed to get around the possible errors emanating from the out-of-plane EF and polarization brought about by the periodic boundary conditions [45]. An external EF application is simulated through a planar dipole sheet introduced at the center of the supercell, as proposed by Neugebauer and Scheffler [46], and implemented in VASP. However, the atomic positions are held fixed under the EF application, which is consistent with earlier works [47–49]. Moreover, Ghosh *et al.* [50] have demonstrated that the structural parameters, i.e., bond length, bond angle, and buckling height, in bilayer blue phosphorous are barely altered by the externally applied EF and interplanar spacing changes by $< 4\%$; however, significant changes in the electronic properties were found under EF applied within the range of 0–0.5 V/Å. The structural modifications are investigated in this paper for the upper limits of the positive and negative EFs. Minor changes are noticed at the strongest positive EF applied, when the structure is allowed to relax, and are not found to change the physics and the understanding. The corresponding results are presented in the Supplemental Material (SM) [51].

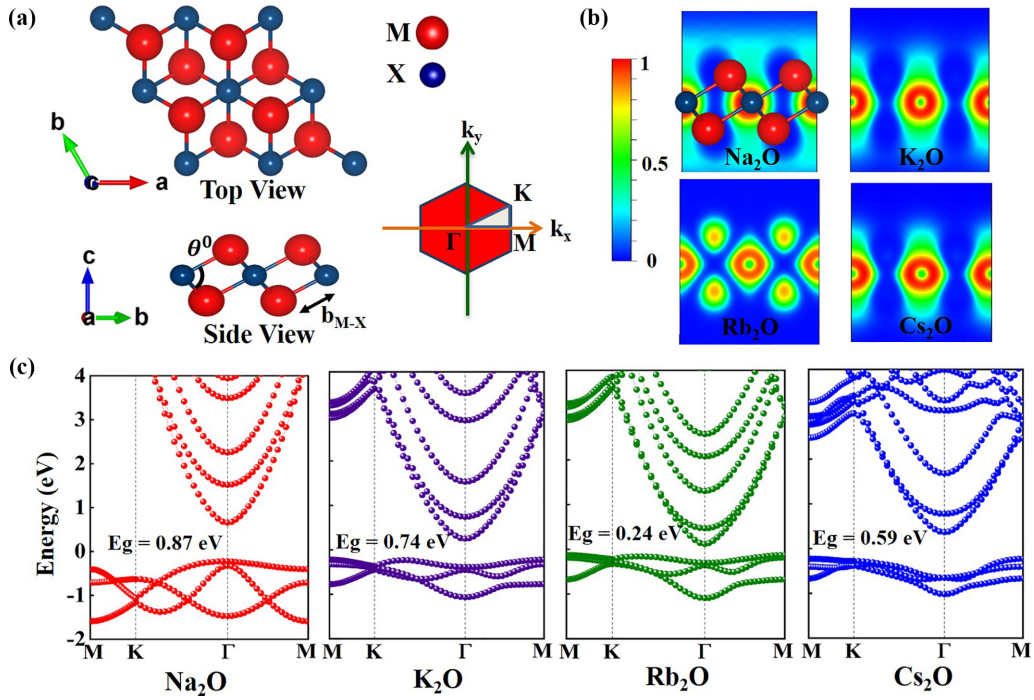

FIG. 1. (a) Top and side views of dialkali monochalcogenides M_2X, where M = Na, K, Rb, or Cs; and X = O, S, Se, or Te. The $b_{M\text{-}X}$ and θ° represent the bond length and the bond angle of the monolayers. (b) Electron localization plot for M_2O (M = Na, K, Rb, and Cs) monolayers. (c) Band dispersion of dialkali monoxide monolayers M_2O (M = Na, K, Rb, and Cs) using the GGA-PBE exchange-correlation functional.

III. RESULTS AND DISCUSSION

A. Relaxed structure of M_2X monolayers

The family comprising 16 monolayers of dialkali metal monochalcogenides M_2X (alkali metal M = Na, K, Rb, or Cs; and chalcogen X = O, S, Se, or Te) is explored in this paper. The primitive unit cell is arranged in an M-X-M pattern with D_{3h} point group symmetry in the $P\bar{6}\,m2$ space group. Figure 1(a) shows the top and side views of the hexagonal honeycomb lattice structure of M_2X monolayers, while Table I lists the relaxed lattice constant, bond length, and bond angle. The lattice parameters are found to be comparable with the earlier reported ones [52,53]. The increase in the bond length and bond angle corresponds with the increasing lattice constant of the M_2X monolayers containing heavier X. The nature of bonding is detected using the electron localization function (ELF), shown in Fig. 1(b). The red, green, and blue regions correspond to maximum (100%), average (50%), and least/zero (0%) probability of tracking the electrons in the region. The maximum (minimum) accumulation on the chalcogen atom (alkali metal), which is negligible on the interatomic distribution, reflects the ionic nature of bonding in the M_2X monolayers. To assure the dynamic stability of the monolayers, the phonon spectra have been inspected. The stability of all the monolayers is shown in Fig. S1 in the SM [51]. Except for a small negative frequency patch near the Γ point, no definite imaginary mode is detected in the Brillouin zone. This small pocket of imaginary frequency is shown by the acoustic flexural (ZA) mode around the Γ point in the phonon spectra. It is a mere artifact in 2D materials, and in some cases, it completely disappears. Reaching numerical convergence for the ZA phonon mode is a common issue in *ab initio* calculations on 2D materials. Small negative frequency pockets (< 0.3 THz or 10 cm^{-1}) around the Γ point caused by ZA modes have also been observed in graphene, silicone, MoS_2, GeSe [54], and indium chalcogenides [55]. This region of instability is especially sensitive to simulation parameters like supercell size and k-point sampling. For these reasons,

TABLE I. The lattice constant (a, b), bond length b_{M-X} of chalcogenide with the alkali metal atom, bond angle θ°, work function ϕ (eV), and band gap E_g (HSE) in eV of the monolayers in the primitive cell.

Monolayer	$a = b$ (Å)	b_{M-X} (Å)	θ°	ϕ (eV)	E_g (HSE)
Na_2O	3.69	2.31	106.00	3.16	1.94
Na_2S	4.45	2.74	108.55	4.13	2.92
Na_2Se	4.67	2.87	108.95	4.23	2.84
Na_2Te	5.03	3.07	109.86	4.35	2.86
K_2O	4.14	2.65	102.38	2.02	1.25
K_2S	4.97	3.11	105.83	3.32	2.46
K_2Se	5.17	3.23	106.09	3.20	2.27
K_2Te	5.53	3.45	106.60	3.54	2.55
Rb_2O	3.33	2.70	95.20	1.65	0.83
Rb_2S	4.44	3.19	101.23	2.53	1.88
Rb_2Se	4.62	3.20	104.87	2.89	2.20
Rb_2Te	4.82	3.50	101.12	3.09	2.34
Cs_2O	4.27	2.89	95.05	1.93	1.23
Cs_2S	5.20	3.38	100.36	2.43	1.75
Cs_2Se	5.42	3.51	100.69	1.33	1.64
Cs_2Te	5.87	3.74	103.23	2.52	1.98

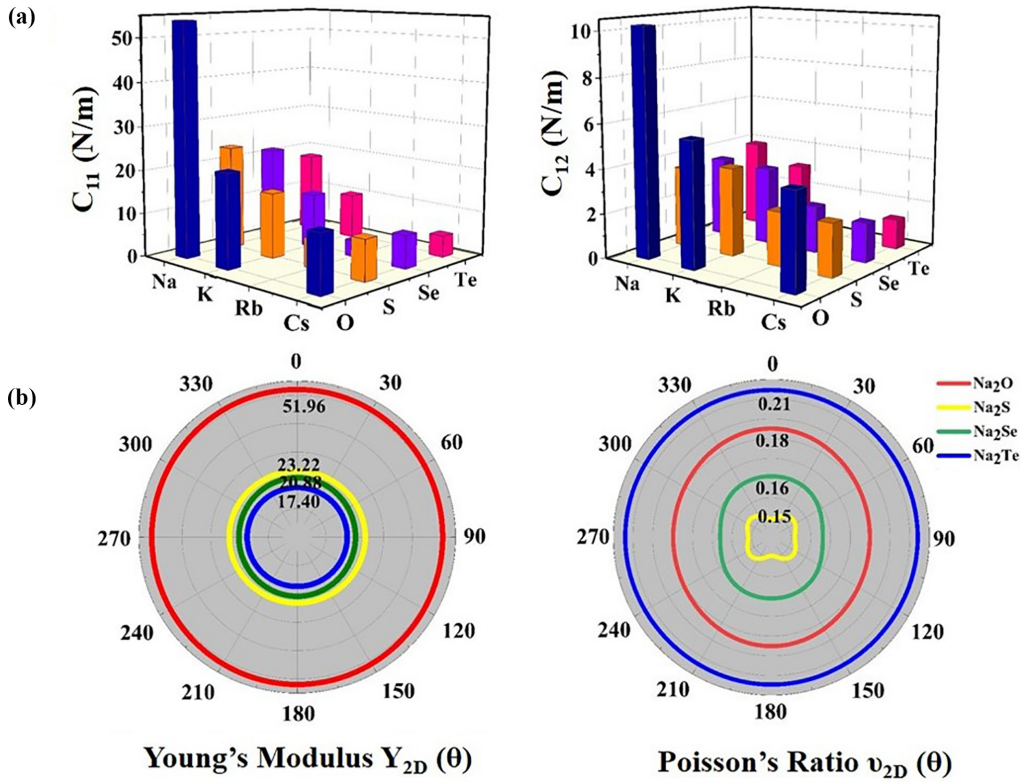

FIG. 2. (a) Elastic constants of M_2X monolayers and (b) the polar plot of Young's modulus Y_{2D} (θ) and Poisson's ratio $\upsilon_{2D}(\theta)$ of disodium monochalcogenide Na_2X (X = O, S, Se, or Te) monolayers.

the negative frequencies are understood to be spurious. Thus, these instabilities are ignorable and thereby confirm the dynamic stability of the monolayers.

The electronic band dispersion for oxide monolayers M_2O (M = Na, K, Rb, or Cs) is calculated using the GGA-PBE functional, as shown in Fig. 1(c), whereas the other monolayers are provided in Fig. S2 in the SM [51]. As the PBE functional expresses the correct band dispersion while underestimating the band gap, a more precise semiconducting band gap energy is attained through the HSE06 functional for all the monolayers and is presented in Table I. Also, the work function for the monolayers has been tabulated in Table I to provide a zeroth-order estimation of the band alignment. From the band spectra given in Fig. 1(c), the primarily parabolic conduction band minimum (CBM) and flat valence band maximum (VBM) dispersion is observed, which would set the lighter electron and bulkier hole mass in the monolayers. The Na_2X monolayers showed a direct band gap, while the higher alkali monolayers M_2X (M = K, Rb, or Cs) presented an indirect band gap. The relocating of the VBM from the Γ point toward the K point has resulted in an indirect band gap in the systems. It has been shown in a prior investigation that the strong p-orbital hybridization between the higher alkali metal and chalcogenide atoms caused the shifting of the VBM and changed the band gap from direct to indirect [52].

B. Mechanical stability and properties

The elastic constants quantify the stiffness of a material. A stiffer material retains its shape for a larger magnitude of applied force or strain. In such cases, a material with less stiffness or smaller Young's modulus (i.e., more flexibility or stretchability) is suitable for flexible electronics. The values of in-plane elastic constants for monolayer M_2X are presented in the bar graph plot in Fig. 2(a). Here, both the ionic and electronic contributions have been summed in the elastic stiffness coefficients. From the elastic constant, all the monolayers of the family are found to be highly flexible. The elastic constants are found to decrease with the higher chalcogen monolayer from O to Te and higher alkali group from Na to Cs in the monolayers. The mechanical stability has been affirmed based on elastic constants of the monolayers. The Born-Huang stability criteria [56] for the hexagonal systems use the following conditions:

$$C_{11} > |C_{12}|, \quad C_{22} > 0, \quad C_{11}C_{22} - C_{12}^2 > 0, \quad C_{66} > 0. \tag{1}$$

All the monolayers entirely satisfy the criteria except for Rb_2O and Rb_2Te monolayers. Thus, for the stable systems, the static in-plane Young's modulus (Y_{2D}) and Poisson's ratio (υ_{2D}) have been calculated through the following expressions:

$$Y_{2D} = \frac{C_{11}^2 - C_{12}^2}{C_{11}}, \tag{2}$$

$$\upsilon_{2D} = \frac{C_{12}}{C_{11}}. \tag{3}$$

The static in-plane Young's modulus and Poisson's ratio have been charted in Table S1 in the SM [51]. Young's

modulus shows the utmost flexibility of the monolayers as compared with the extensively studied graphene (Y_{2D} = 341 N m^{-1}) [57], MoS_2 (Y_{2D} = 130 N m^{-1}) [58,59], and h-BN (Y_{2D} = 275.9 N m^{-1}) [60]. The values are comparable with Young's modulus of silicene (61 N m^{-1}), Janus SnSSe (57.5 N m^{-1}), and germanene (41 N m^{-1}) [61]. Poisson's ratios detected are < 0.5, which attested the feasible compressibility of the monolayers.

The orientational Young's modulus Y_{2D} (θ) and Poisson's ratio ν_{2D} (θ) are investigated to find the nature of mechanical properties in the system, using the following relations [62]:

$$Y_{2D}(\theta) = \frac{C_{11}C_{22} - C_{12}^2}{C_{11}s^4 + C_{22}c^4 + \left(\frac{C_{11}C_{22}-C_{12}^2}{C_{66}} - 2C_{12}\right)c^2s^2}, \quad (4)$$

$$\nu_{2D}(\theta) = \frac{C_{12}(s^4 + c^4) - \left(C_{11} + C_{22} - \frac{C_{11}C_{22}-C_{12}^2}{C_{66}}\right)c^2s^2}{C_{11}s^4 + C_{22}c^4 + \left(\frac{C_{11}C_{22}-C_{12}^2}{C_{66}} - 2C_{12}\right)c^2s^2}, \quad (5)$$

where s and c are sinθ and cosθ, and θ is the polar angle along the armchair axis. The orientation-dependent plot presented in Figs. 2(b) and S3 in the SM [51] confirms the isotropy in Young's modulus Y_{2D} (θ) of Na_2X (X = O, S, Se, or Te) and other monolayers of the family, which is quite observable in hexagonal symmetry structures [63]. Also, Poisson's ratio ν_{2D} (θ) is found to be quite isotropic except for a little anisotropy in Na_2S and K_2Se.

C. Piezoelectricity

With the broken inversion symmetry and high flexibility of the monolayers, piezoelectricity is expected to arise. The piezoelectric tensor coefficients have been determined using DFPT integrated into VASP. The e_{ij} piezoelectric stress tensor is attained by the summation of the ionic and electronic terms e_{ij}^{ionic} and $e_{ij}^{\text{electronic}}$, respectively.

A three-rank piezoelectric stress tensor e_{ijk} is expressed as

$$e_{ijk}^{\text{elec}} + e_{ijk}^{\text{ion}} = \left(\frac{\partial P_i}{\partial \varepsilon_{jk}}\right)_{E,T}, \quad (6)$$

and a three-rank piezoelectric strain tensor d_{ijk} as

$$d_{ij}^{\text{elec}} + d_{ij}^{\text{ion}} = \left(\frac{\partial P_i}{\partial \sigma_{jk}}\right)_{E,T}, \quad (7)$$

where E_i, P_i, ε_{jk}, T, and σ_{jk} are the macroscopic EF, electric polarization, strain tensor, the temperature in Kelvin, and stress tensor. Here, i, j, and k represent the x, y, and z or 1, 2, and 3 directions. The piezoelectric tensors can be correlated as

$$e_{ijk} = \frac{\partial P_i}{\partial \varepsilon_{jk}} = \frac{\partial P_i}{\partial \sigma_{mn}}\frac{\partial \sigma_{mn}}{\partial \varepsilon_{jk}} = d_{imn}C_{mnjk}. \quad (8)$$

The D_{3h} point group symmetric structures do not maintain the exclusiveness of the piezoelectric tensor coefficient. In this case, employing Voigt notation for the 2D materials, the third-rank piezoelectric tensors can be reduced to second rank by the contraction of the cartesian coordinates as 11 $\rightarrow$ 1, 22 $\rightarrow$ 2, 33 $\rightarrow$ 3, 23 $\rightarrow$ 4, 13 $\rightarrow$ 5, and 12 $\rightarrow$ 6, resulting in a 3 $\times$ 6 matrix [16,64,65]:

$$e_{111} = e_{11} = -e_{211} = -e_{112} = e_{22} = -e_{21} = -e_{16} = e_{331} = e_{322} = e_{31} = e_{32},$$

$$e_{113} = e_{223} = e_{15} = e_{24},$$

The symmetry analysis reduces the number of independent elastic tensor components:

$$\sigma_{ij} = \sigma_{ji},\ C_{ijkl} = C_{jikl}, \quad (9)$$

$$\varepsilon_{kl} = \varepsilon_{lk}, C_{ijkl} = C_{ijlk}. \quad (10)$$

Further the strain energy $U = \frac{1}{2}C_{ijkl}\,\varepsilon_{ij}\varepsilon_{kl}$ with the property $\frac{\partial U}{\partial \varepsilon_{ij}} = \sigma_{ij}$ then with all the symmetries:

$$C_{ijkl} = C_{jikl},\ C_{ijlk} = C_{jilk}\ C_{ijkl} = C_{klij}. \quad (11)$$

This resulted in a contracted notation $\sigma_i = C_{ij}\varepsilon_j$.

From the above representations, the contracted piezoelectric stress and strain tensors are linked by elastic stiffness tensor C_{ij} as

$$e_{ij} = d_{ik}C_{kj}. \quad (12)$$

The piezoelectric stress and strain coefficients originate from the piezoelectric polarization, i.e., polarization induced upon the application of infinitesimal strain or stress. According to Dong *et al.* [20], in vdW crystals, out-of-plane piezoelectric strain coefficient d_{33} can be reasonably approximated as

$$d_{33} = \frac{(C_{11} + C_{12})e_{33} - 2C_{13}e_{31}}{(C_{11} + C_{12})C_{33} - 2C_{13}^2} \approx \frac{e_{33}}{C_{33}}. \quad (13)$$

The piezoelectric coefficients of the monolayers determined in the out-of-plane direction have been tabulated in Table II. The flexible M_2X monolayers of the family are found to exhibit small negative out-of-plane piezoelectric stress and strain coefficients e_{33} and d_{33}. In the earlier studies, the individual monolayers of the heterostructures BP/GaN

TABLE II. Piezoelectric stress coefficient (e_{33}), elastic stiffness constants (C_{33}), and out-of-plane piezoelectric strain coefficient (d_{33}) of dialkali metal monochalcogenide monolayers.

2D monolayer	e_{33} (pC m^{-1})	C_{33} (N m^{-1})	d_{33} (pm V^{-1})
Na_2O	21.61	1.751	1.45
Na_2S	0.00	0.192	0.00
Na_2Se	0.00	0.133	0.00
Na_2Te	−0.51	0.52	−1.09
K_2O	−0.19	1.694	−0.11
K_2S	0.05	0.129	0.2
K_2Se	0.05	0.016	−2.8
K_2Te	0.03	0.027	−1.5
Rb_2S	−0.03	0.063	−0.51
Rb_2Se	−0.03	0.054	−0.63
Cs_2O	0.00	0.340	0.00
Cs_2S	−0.06	0.251	−0.25
Cs_2Se	−0.04	0.072	−7.81
Cs_2Te	−0.07	0.13	−0.51

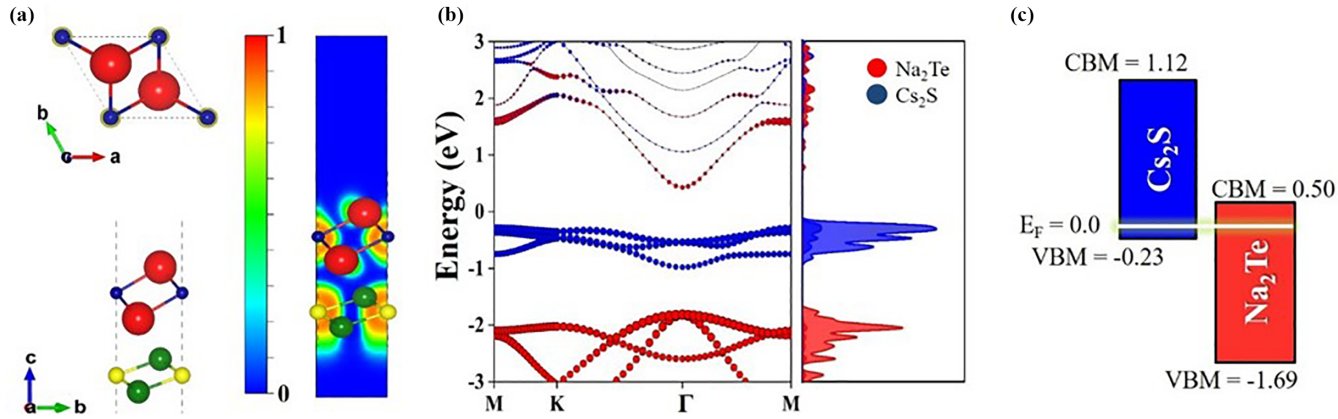

FIG. 3. (a) Top and side views of Na_2Te/Cs_2S heterobilayer and its electron localization function (ELF) plot. (b) Band structure and density of states plot with individual monolayer contribution to the band dispersion. (c) Band alignment in Na_2Te/Cs_2S heterobilayer.

[19] and In_2Se_3/MoS_2 [15] showed no or small strength of piezoelectricity along the z direction, but the vdW structures formed witnessed multifold enhancement in piezoelectricity. Thus, with a view to improving upon the piezoresponse of the family of monolayers, 2D type-II vdW heterostructures have been built up by stacking monolayers on top of one another. The vdW heterostructures with lattice mismatch $<$ 4% have been investigated for their piezoelectric properties, where the Na_2Te/Cs_2S heterostructure manifested the highest out-of-plane piezoelectric response. The maximum piezoelectric strain response observed in the Na_2Te/Cs_2S system is $d_{33} = -39$ pm V^{-1}, respectively. The responses of other heterostructures of the family are shown in Fig. S4 in the SM [51]. The anomalous negative piezoelectric response in heterostructures is scarcely observed. Thus, its origin needs to be elucidated to benefit from this property in future applications. The coming sections are devoted to a thorough investigation of the electronic, mechanical, interfacial charge polarization, electrostatic potential, and piezotronics properties along with the response of the vertical strain and out-of-plane EF applied on the system.

D. High negative piezoelectricity in Na_2Te/Cs_2S vdW heterostructure

1. Geometric and electronic properties

The heterostructure is formed by putting together the individual monolayers vertically in the AA stacking arrangement with the weak vdW interaction holding the monolayers on top of each other. Nearly 3.24% lattice mismatch is found between the individual monolayers in the supercell for the vdW heterostructure, which ensures that the properties of the constituent monolayers are insignificantly altered under this small magnitude of strain. Figure 3(a) provides the top and side views of the optimized heterostructure where the red, blue, yellow, and green spheres represents Cs, S, Te, and Na atoms. The optimized lattice constant and interlayer distance are 5.06 and 2.61 Å, respectively. In the electron localization plot shown in Fig. 3(a), the red 1 represents the 100% electron density, and the blue 0 indicates 0% electron density in the region. The maximum (minimum) electron localization is found to occur on the chalcogen (alkali) atoms, which clearly depicts the ionic bonding in the intralayer Na_2Te and Cs_2S monolayers of the vdW heterostructure.

The electronic band structure of the Na_2Te/Cs_2S heterostructure computed using the PBE functional shows an indirect band gap of 0.73 eV with the CBM and VBM lying at the high-symmetry Γ and M points, respectively. The well-known underestimation in the band gap by the PBE functional has prompted the use of a more precise HSE06 functional to determine a more accurate band gap of 1.36 eV in the Na_2Te/Cs_2S heterostructure. The band dispersion and DOS presented in Fig. 3(b) show the proper band contribution by the individual monolayers Na_2Te and Cs_2S. Figure 3(b) reveals the dominant contribution of the bands of Na_2Te (Cs_2S) to the CBM (VBM) band in the heterostructure, thus asserting the type-II band alignment in the system. A comparison in the band structure between the heterostructure and the individual monolayers Na_2Te and Cs_2S barely reveals any changes from the constituent monolayers to that in the heterostructure, as shown by Fig. S5 in the SM [51]. It indicates the ability of the individual monolayers to retain their identity while constructing the heterostructure. The band alignment of the monolayers displayed in Fig. 3(c) shows a substantial band offset of 0.6 and 1.4 eV in the CBM and VBM, respectively, in the Na_2Te/Cs_2S heterostructure. The occurrence of a large band offset in the system can imply a vast potential for the application of the layered structure [66]. This much higher band offset among the monolayers would result in an intense interlayer charge polarization and can drive a large out-of-plane piezoelectric response in the heterostructure. In an earlier investigation on the In_2Se_3/MoS_2 heterostructure, the enhanced piezoelectricity arose from the large band offset of 0.8 eV between the monolayers of the constituents. However, the independent monolayers exhibited a very low piezoelectric response [15]. Thus, a larger band offset in the Na_2Te/Cs_2S heterostructure is expected to bring in the emerging piezoelectric response through the interface effects between the individual layers.

2. Mechanical flexibility and stability

The 2D elastic moduli of the vdW Na_2Te/Cs_2S heterobilayer are shown in Table III. The magnitude of in-plane

TABLE III. The elastic stiffness constants, Young's modulus (Y), Poisson's ratio (υ), and bending modulus (D) of the heterostructure.

Heterostructure	$C_{11} = C_{22}$	C_{12}	$C_{66} = G$	C_{33}	Y (N m^{-1})	υ	D (eV)	Status
Na_2Te/Cs_2S	26.54	9.87	7.28	2.56	22.86	0.37	8.83	Stable

elastic moduli C_{11} in a vdW bilayer is observed to be close to the sum of the elastic moduli of the constituent monolayers. The C_{11} moduli in the heterobilayer is usually lower [59,67–69] or higher [70–73] than the sum of the individual ones depending upon the strength of the vdW interaction between the monolayers, which is quantifiable via the out-of-plane elastic constant C_{33}. The interlayer coupling at the interface of layers stacked by the vdW interaction enhances C_{33} in the bilayer relative to the individual monolayers [74,75], as given in Table IV. Also, by varying the interlayer distance, its effects on in-plane and out-of-plane elastic constants have been understood, as given in Table S2 in the SM [51]. The interlayer coupling or interaction clearly increases with the decrease in interlayer distance, which evidently shows up in the increases in C_{33} and, in turn, a higher in-plane elastic constant, i.e., C_{11}. The Na_2Te/Cs_2S heterostructure meets all the Born-Huang elastic stability criteria for the hexagonal system, i.e., $C_{11} > |C_{12}|$, $C_{22} > 0$, $C_{11}C_{22} - C_{12}^2 > 0$, and $C_{66} > 0$:

$$Y_{2D} = \frac{C_{11}^2 - C_{12}^2}{C_{11}}; \quad \upsilon = \frac{C_{12}}{C_{11}}; \quad G = C_{66}; \quad D = \frac{Yh^2}{12(1-\upsilon^2)}. \tag{14}$$

The in-plane static Young's modulus (Y) is of lesser order than that of the numerous flexible monolayers [76,77]. Also, the bending modulus is comparable with monolayer WSe_2 ($D = 8.5$ eV) [78] and MoS_2 [79], affirming the robust mechanical properties of the heterostructure.

To determine any anisotropy present in the vdW heterobilayer (vdWH), the area modulus (K^V and K^R) and shear modulus (G^V and G^R) have been calculated using the Voigt and Reuss estimation by the following formulas [80]:

$$K^V = \frac{C_{11} + C_{22} + 2C_{12}}{4}, \tag{15}$$

$$K^R = \frac{1}{S_{11} + S_{22} + 2S_{12}}, \tag{16}$$

$$G^V = \frac{C_{11} + C_{22} - 2C_{12} + 4C_{66}}{8}, \tag{17}$$

$$G^R = \frac{2}{S_{11} + S_{22} - 2S_{12} + S_{66}}, \tag{18}$$

TABLE IV. Piezoelectric stress coefficient (e_{33}), elastic stiffness constants (C_{33}), and out-of-plane piezoelectric strain coefficient (d_{33}) of Na_2Te/Cs_2S heterostructure. The units of e_{il}, C_{ij}, and d_{il} are pC m^{-1}, N m^{-1}, and pm V^{-1}, respectively.

Material	e_{33}	C_{33}	d_{33}
Na_2Te/Cs_2S heterobilayer	−59.68	2.56	−39.89
Cs_2S bilayer	−16.43	8.35	−2.028
Na_2Te bilayer	−4.342	3.15	−1.92

where C_{ij} are elastic stiffness constants, S_{ij} are compliance matrices defined as $S = C^{-1}$. The calculated area and shear modulus are estimated to be $K^V = 18.21$ eV, $K^R = 18.28$ eV, $G^V = 7.81$ eV, and $G^R = 7.73$ eV. The elastic anisotropy index indicating the degree of anisotropy in the system has been determined from the area and shear modulus using the following relation:

$$A^{SR} = \sqrt{\left(\frac{K^V}{K^R} - 1\right)^2 + 2\left(\frac{G^V}{G^R} - 1\right)^2}. \tag{19}$$

The A^{SR} comes out to be 0.014 which is extremely close to zero. The minimum value of the elastic anisotropy index for an isotropic system can reach zero in the case of perfect mechanical isotropy in the system. Thus, the vdWH has been found to retain isotropic elastic properties in the individual monolayers.

3. Electrostatic potential and interfacial charge transfer in 2D layered heterostructure

Despite weak vdW contact within the stacked monolayers, there lies possibilities for interlayer charge exchange or polarization, either due to the small interlayer spacing/gap or high electronegativity difference between the individual layers. To shed light on the interfacial properties of the heterostructure, the electrostatic potential and interfacial electrostatic charge distribution have been explored. The average electrostatic potential of the individual monolayers and the heterostructure Na_2Te/Cs_2S has been calculated in an absolute vacuum scale, as shown in the Fig. 4. The potential plot of the constituent monolayers relative to the constructed heterobilayer hardly indicates any difference, owing to the weak vdW interaction existing between the individual monolayers. The difference in electrostatic potential between the heterostructure and the sum of the potential of the two monolayers is indicated by potential energy difference ΔV at the interface, which brings about the built-in EF. The deformation charge density or the planar averaged charge density difference ($\Delta\rho$) can quickly unveil the electronic charge redistribution across the monolayers using following formalism [81]:

$$\Delta\rho = \int \rho_{Na_2Te/Cs_2Te}(x,y,z)dxdy - \int \rho_{Na_2Te}(x,y,z)dxdy - \int \rho_{Cs_2Te}(x,y,z)dxdy, \tag{20}$$

where ρ is the plane averaged charge density of the vdWH and monolayers. The oscillating deformation charge density ($\Delta\rho$) or the alternating spatial charge accumulation and depletion, shown in Fig. 4(b), indicates the charge polarization, instigated by the built-in EF in the system. On average, Na_2Te and Cs_2S monolayers get negatively (in red) and positively (in green) charged by the vdW interactions. The extent of charge acquired/transferred has been quantified by the integration

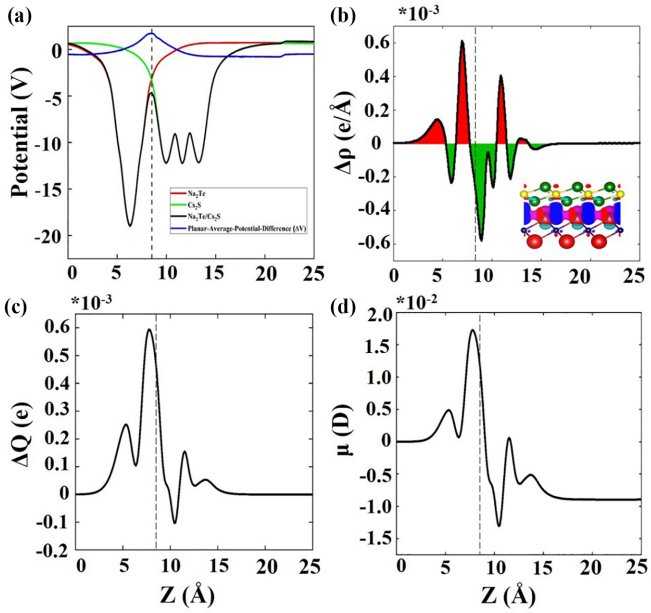

FIG. 4. (a) Potential energy distribution. (b) Plane-averaged charge density difference. Here, the oscillations show depletion and accumulation (in green and red) of electronic charge density, and the inset three-dimensional (3D) isosurface of charge density difference. (c) Total charge transferred. (d) Interfacial dipole moment μ in the normal plane of the Na_2Te/Cs_2S heterostructure.

of the charge density difference as $\Delta Q = \int_{-\infty}^{Z} \Delta\rho(z')dz'$, where $\Delta\rho$ is the planar average charge density difference for the heterostructure. From Fig. 4(c), the Na_2Te monolayer is observed gaining $\Delta Q = |0.015|e$ charge from the Cs_2S layer. The small degree of charge transfer or polarization confirms the weak character of the vdW interaction. Further, the interface-induced dipole moment by the charge transfer has been determined using $\mu = \int_{-\infty}^{Z} z\Delta\rho(z')dz'$. Formation of the dipole moment of -0.008 D strength in the heterostructure is observed, where the negative values of μ suggest the outward pointing dipole [82], that is, from Na_2Te to Cs_2S monolayer. The development of large electrostatic potential energy difference, oscillating deformation charge density, and built-in interfacial dipole moment in the z direction will assuredly lead to out-of-plane polarization and resultant out-of-plane piezoelectric coefficient in the heterostructure.

4. Piezoelectricity

The piezoelectric stress and strain coefficients for the heterobilayer Na_2Te/Cs_2S have come out to be $e_{33} = -200.8$ pC m^{-1} and $d_{33} = -39$ pm V^{-1}, respectively. The interface effects in vdW bilayers enhance the piezoelectric coefficient d_{33} with respect to the individual monolayers [15,19,83,84]. In addition, the variation in piezoelectric response with different stacking arrangements by rotating one monolayer about another at angles of 0°, 60°, 120°, and 180° is shown in Fig. S8 and thoroughly discussed in the SM [51]. Further, to observe the heterostructure vs the influence of layering, piezoelectric studies have been carried out on individual bilayers of Na_2Te and Cs_2S, where interfacial characteristics comprising electrostatic potential, planar averaged charge density, charge transfer, and development of the dipole moment at the interface have been computed, as shown in Figs. S6 and S7 in the SM [51]. In both homobilayers and heterobilayers of Na_2Te and Cs_2S, the elastic stiffness C_{33} is noted to be higher than the individual monolayers, as given in Table IV, due to the presence of the vdW interactions at the interface which is common in layers stacked via weak vdW interactions [74,75].

Then the piezoelectric coefficients (e_{33} and d_{33}) are found to be enhanced in the bilayers and heterostructure with respect to the individual monolayers due to interface effects (i.e., through the development of interfacial dipoles) [19,31–34]. As the charge transfer and polarization (electronic dipole) arises at the interface, as marked with the dashed line in Figs. 4 and S6 and S7 in the SM [51], piezoelectricity increases correspondingly in bilayer Na_2Te, bilayer Cs_2S, and the Na_2Te/Cs_2S heterobilayer, depending on the sensitivity of the interfacial polarization to the application of infinitesimal stress or strain, as calculated using DFPT. The maximum piezoelectric stress and strain coefficients in the Na_2Te/Cs_2S bilayer are apparently caused by its smaller C_{33} and higher interfacial charge polarization relative to the other bilayers. The higher charge polarization is brought about by a higher ΔV and is indicated by higher charge transfer (ΔQ) and higher interfacial dipole moment (μ) at the interface, i.e., in the neighborhood of the vertical dotted lines in Figs. 4 and S6 and S7 in the SM [51]. Finally, it is the piezoelectric polarization and not the intrinsic polarization which is responsible for the piezoelectric constants obtained through DFPT calculations in this paper. The change in polarization under infinitesimal stress or strain, i.e., piezoelectric polarization, is understood to be higher in the heterobilayer than the homobilayers, as confirmed by the higher values of e_{33} and d_{33} obtained from the DFPT calculations.

In a strong out-of-plane piezoelectric coefficient, its sign should not be neglected. The anomalous negative piezoelectricity in the heterostructure can bring about an uncommon response, leading to the interlayer compression along the direction of the applied EF, as opposed to the usual crystal expansion in a material having positive piezoelectric coefficient. A thorough investigation of the heterostructure will determine the origin of such anomalous behavior in the system. To probe the nature of the vdW interaction, the in-plane stress induced in the heterostructure by vertical compressive strain has been examined, as shown Fig. 5(a). The linear fit to the stress-strain curve in the range of 3% strain has given the out-of-plane Young's modulus to be 11 N m^{-1}. The extremely small Young's modulus is in sync with the small out-of-plane elastic constant C_{33}. Hereafter, the impact of strain on interlayer vdW distance d and intralayer thickness g has been plotted in Fig. 5(b). The larger influence on intralayer vdW distance d relative to ionically bonded intramonolayer thickness g with strain is found in the heterostructure, which appears due to the soft vdW interaction in the system. The ferroelectric polymer PVDF and its copolymers, which condense through the weak van der Waal interaction, exhibit negative piezoelectricity. In experimental and theoretically examined 2D $CuInP_2S_6$, the free movement of Cu ion and the soft interaction offer large deformation under EF and bring out negative piezoelectricity in the system. The anomalous negative

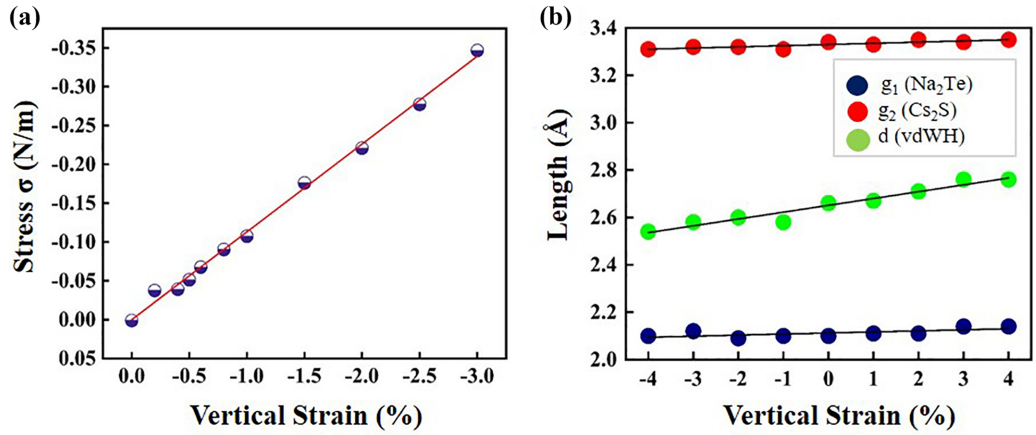

FIG. 5. (a) Stress-to-strain plot under vertical compressive strain. (b) Change in layer thickness g_1 (Na-Na), g_2 (Cs-Cs), and interlayer van der Waals distance d (Na_2Te-Cs_2S) with the vertical compressive and tensile strain.

piezoelectric responses in the Na_2Te/Cs_2S heterostructure have stemmed from the small Young's modulus, elastic constant C_{33}, and the soft interactions at the interface. This unconventional piezoelectric coefficient in the heterostructure will establish applications in futuristic electromechanical piezoelectric devices at the nanoscale.

5. Vertical compressive strain

The application of vertical compressive strain is an effectual mean to vary the electronic band spectra of 2D systems. The earlier studies on graphene [85], $MoTe_2$, WTe_2 monolayers, and their heterostructures [86] have shown the band gap opening under compressive strain. The application of strain by changing interlayer equilibrium distance significantly varies the interlayer interaction in the heterostructure and modifies the electronic properties of the system. By reducing the interlayer gap in the heterostructure, the Coulombic repulsion between the individual layers sets in first, which increases progressively and results in the change in electronic properties like band structure and band gap attenuation. Here, the investigation has been conducted on the heterostructure Na_2Te/Cs_2S to observe the influence of strain on the electronic properties of the system. Interlayer gap smaller than the equilibrium interlayer distance d_0 turns the binding energy of the heterostructure positive and thus brings it to the repulsive regime, which can be seen in Fig. 6(a). The increasing interlayer distance beyond $d > d_0 = 2.61$ Å results in band gap reduction, while the decreasing interlayer distance $d < d_0$ enlarges the band gap. The increasing binding energy or the interlayer Coulomb repulsion together with the hybridization of orbitals from each layer by vertical compressive strain causes the increase in band gap in the heterostructure which is comparable with the earlier findings on the heterostructures C_2N/MoS_2 [87], graphene/$PtSe_2$ [88], and graphene/MgS [48]. The band dispersion clearly displays the movement of the energy band with the strain. In the Figs. 6(b) and 6(c), the electronic band structures at the interlayer gap $d-d_0 = 0.6$ and -0.6 Å has been shown where the influence of the strain is clearly discernible at the CBM of the heterostructure, which induces the modulation in band gap. The work function and band alignment along the side undergo some changes under vertical strain. The CBM moves up (down) upon decreasing (increasing) the interlayer distance. However, the type-II band alignment arising from CBM (VBM) contributed by Na_2Te (Cs_2S) monolayers is found to be retained even at the highest level of vertical strain studied in this paper. The work function is a bit sensitive to the application of interlayer distance, as tabulated in Table S2 in the SM [51], where compressive (tensile) strain is found to increase (decrease) the work function. Additionally, the magnitude of the planar average electrostatic potential rises (falls) at the interlayer region upon decrease (increase) in interplanar spacing/distance. As a result, it induces a higher (smaller) charge polarization and dipole under compression (expansion) of the interlayer distance. Consequently, the difference in charge density shows a similar trend and is consistent with the behavior in work function. Figure S9 in the SM [51] shows the planar-averaged electrostatic potential energy distribution, the plane-averaged charge density difference, total charge transferred, and the interfacial dipole moment μ for the Na_2Te/Cs_2S heterostructure with the change in interlayer distance (d-$d_0 = -0.6$, 0, and 0.6 Å). This band gap tunability via the applied vertical strain can in fact present greater opportunities for the heterostructure in the fields of nanoelectronics, piezotronics, optoelectronics, etc.

6. External EF

(a) Energy band diagrams. External EF on a low-dimensional material is hot stream work and is seen bringing huge improvements to the electronic properties of the systems. Experimentally, multilayer MoS_2 has been reported, showing the transition in the band gap from indirect to direct with the EF. Other monolayers, for instance, MX_2 (M = Mo or W; and X = S, Se, or Te) [89], MgTe [14], Janus SnSSe [90], heterostructure SiC/BN [91], and α-P/H-MoS_2 [92], have come up with band gap closing by EF. The evaluation of the band gap in the presence of an EF is a vital investigation that should be conducted to forecast the potential of 2D systems in low-powered devices.

The EF effects on the Na_2Te/Cs_2S heterostructure have been investigated to study the electronic property modulation in the system. The field is applied normal to the plane in the range of $+0.4$ to -0.4 V/Å. The equilibrium structure is

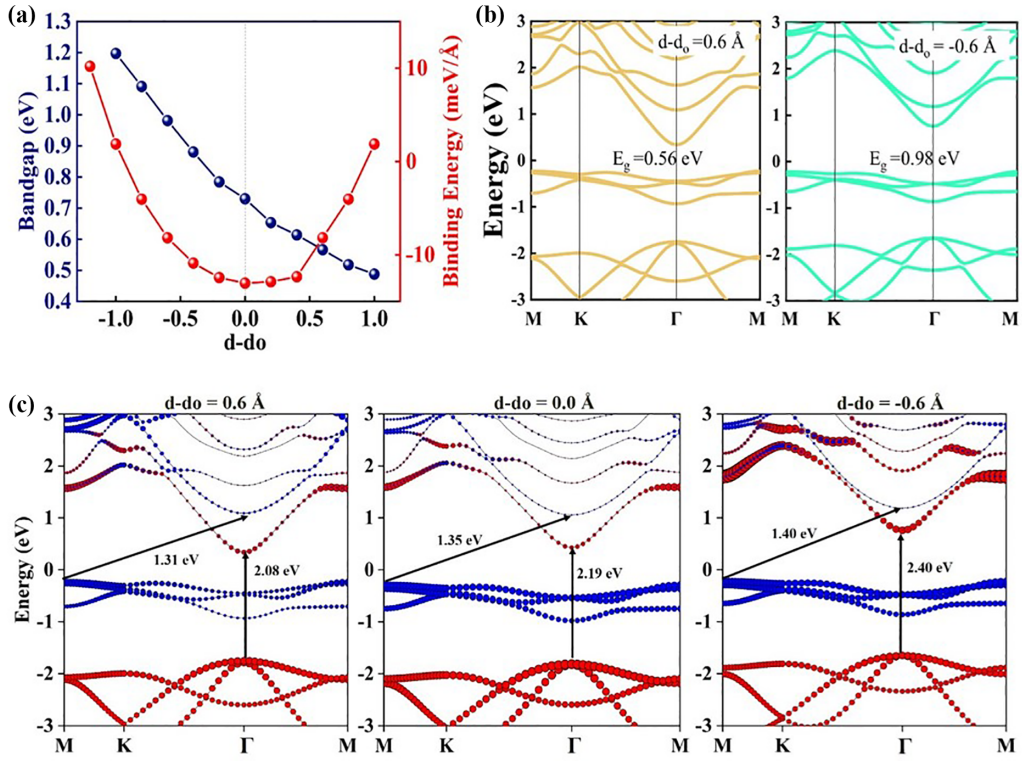

FIG. 6. (a) Change in band gap and binding energy of Na_2Te/Cs_2S heterostructure with the change in interlayer distance from equilibrium. (b) Band structure evolution in Na_2Te/Cs_2S heterostructure at the changed interlayer distance $d-d_0 = 0.6$ and -0.6 Å. (c) Band dispersion under strain showing the contribution of Na_2Te (red) and Cs_2S (blue) monolayers.

preserved throughout the application of the EF. The electronic structure evolution with the EF, shown in Fig. 7(a), exhibits a decrease in band gap with the increasing EF strength. The band gap falls gradually with the negative EF and reaches zero at the field strength of -0.33 V/Å, while for the positive EF, it initially increases up to 0.88 eV and then starts decreasing and completely closes at $+0.31$ V/Å field. At high EFs (0.31 and -0.33 V/Å), minor change occurs upon structural relaxation, which has been tabulated in Table S3 in the SM [51]. At the applied EF of 0.31 V/Å, the interlayer distance changes by only 0.48 Å. The band structure is hardly found to be altered by this structural change under the applied vertical EF of 0.31 V/Å. A slight change in the band gap is noted upon relaxing the structures, as follows. The EF (along the z direction) needed for closing the band gap is found to increase only by 0.03 V/Å. While the band gap is unaffected by an EF of magnitude -0.33 V/ applied along the $-z$ direction. A comparative study of the relaxed and unrelaxed structures under the influence of the EF, as plotted in Fig. S10 in the SM [51], hardly shows any difference in the band structures. It clearly indicates that the underlying physics does not change from the unrelaxed to the relaxed structure at the high value of EF ~ 0.3 V/Å.

A gradual transition from semiconduction to metallization in the vdWH by the EF along both directions can purposely serve the heterostructure in the field of digital electronics. As at zero EF, the heterostructure is semiconducting with high resistance and low tunneling current (OFF state), whereas at critical EF of $+0.31/-0.33$ V/Å, it is metallic with low resistance and high tunneling current (ON state). The output response can be simply tuned from ON to OFF state (1 to 0) and vice versa through a low gate voltage. In Fig. 7(c), a schematic of the ON/OFF state with the pulsed input voltage has been presented. Like this, the heterostructure can be considered for data storage device applications where gate voltage can easily control the output signal.

On visualizing the band spectra, the change in the band gap from the semiconducting to the metallic state is clearly visible to be driven by the NFEG bands in the Na_2Te/Cs_2S heterostructure. The blue, red, and black bands show the Cs_2S, Na_2Te, and NFEG bands in the electronic dispersion in Fig. 7(a). The NFEG states are the unoccupied surface states on the 2D materials with nearly free electronlike characteristics. As these states are extremely sensitive to external perturbations, it can be brought down to around the Fermi level via the effect of EF or surface functionalization [29,93,94] and then used advantageously in surface catalysis, sensing, and increasing the electrical conductivity of the heterostructure [95]. Any possible errors occurring in the energetic position and spatial location of these states in the presence of an EF can be addressed through the application of the periodic boundary condition together with a dipole correction term [45], as employed in this paper. However, in this paper, the NFEG states are visible in the single-layer Cs_2S monolayer even when no EF is applied. The occurrence of NFEG states in the single layer of Cs_2S even in the absence of an applied EF completely rules out the possibility of computational artifacts in the emergence of these states. Figure S13 and the discussion that follows it in the SM [51] support this argument assertively. In this paper, we demonstrate

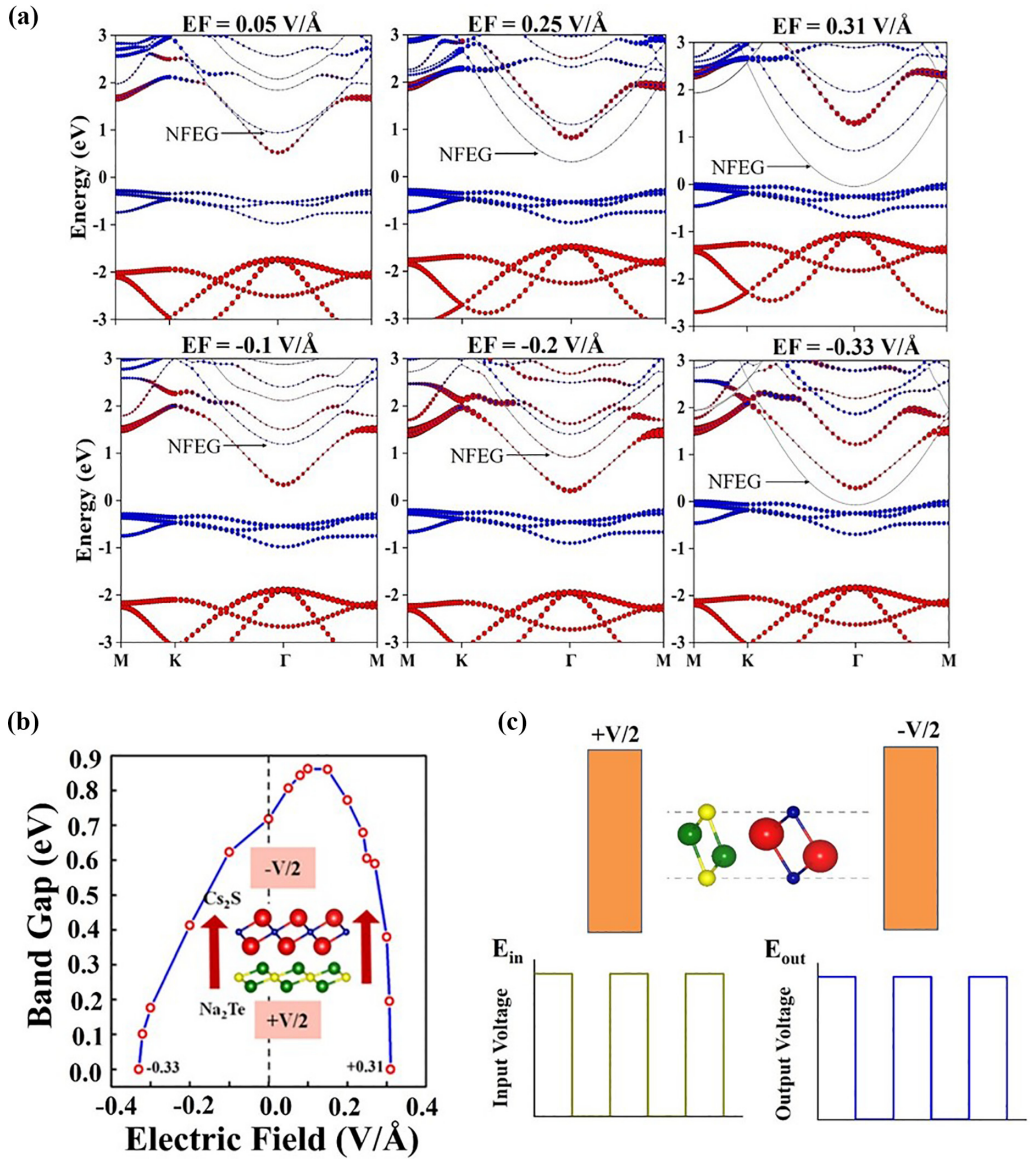

FIG. 7. (a) Band dispersion under the application of positive and negative out-of-plane electric field [EF; the nearly free electron gas (NFEG) states have been indicated by arrows]. (b) Band gap modulation via the EF for the heterostructure. (c) Schematics illustration of the application of out-of-plane EF and electric output response by modulating the electric input.

unequivocally that the NFEG states are truly physical and not artifacts of the calculations, as has been observed theoretically and experimentally in certain other 2D systems [29,30,32,96–98].

From Fig. 7(a), the dominance of the NFEG bands with the increasing EF in either direction can be grasped. They overshoot the CBM at a higher field strength and ultimately fall to the Fermi level, resulting in zero band gap of the heterostructure. To investigate the response of NFEG states to an applied EF, the electronic band structure at different field strengths around the high-symmetry Γ point has been depicted in Fig. S11 in the SM [51]. The NFEG band, which is a conduction band, as marked by arrows in Fig. S11 in the SM [51], evolves with positive and negative EF. The spatial distribution of the NFEG states in the Na_2Te/Cs_2S heterostructure, shown in Fig. S12 in the SM [51], is given by the band-decomposed charge density at the Γ point in the marked conduction band in Fig. S11 in the SM [51]. The NFEG charge density peak is observed close to the Cs_2S monolayer in the absence of applied EF, which is consistent with the contribution of the Cs_2S monolayer to the NFEG states at zero EF, as supported by the atom projected band structure of the NFEG band. It is like the contribution of hydrogen atoms to NFEG states in $Hf_2C(OH)_2$ [29]. Upon the application of EF of progressively increasing strength to the heterostructure, the NFEG state density is found to shift away to the vacuum region for both positive and negative EFs, and consequently, the contribution of the Cs_2S monolayer to the NFEG band gradually drops off and vanishes for both positive and negative EFs, as evident from the atom projected band structure. The trend is found to be the same for both positive and negative EFs. The dropping of the NFEG states upon the application of an EF has been noticed in a bilayer InSe [31]. Also, Shibuta *et al.* [99] studied the NFEG bands

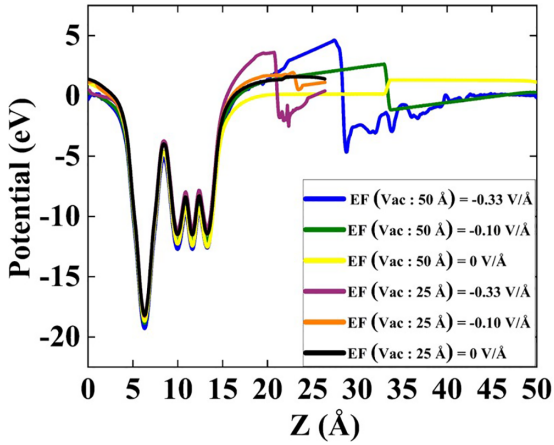

FIG. 8. Change in electrostatic potential with applied electric field at vacuum thicknesses of 25 and 50 Å.

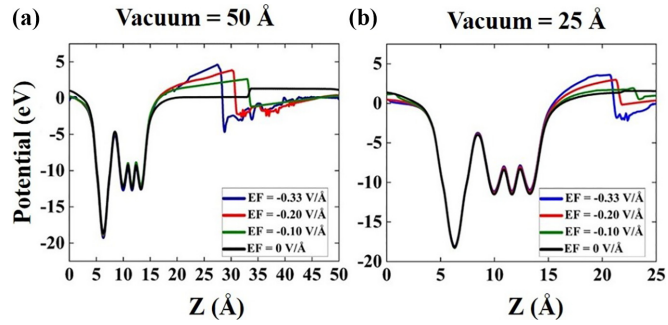

FIG. 9. Electrostatic potential as a function of applied electric field in Na_2Te/Cs_2S heterostructure with a vacuum thickness (a) 50 Å and (b) 25 Å.

above the Fermi level, where they observed a pronounced charge transfer on the lowering of these bands. Interestingly, in MoSSe/BP and InSe/BP heterobilayers [49,84], the results vary from the current heterostructure. On the application of positive and negative EFs, the bands of the individual monolayers move along opposite directions to close the band gap at unequal magnitudes of positive and negative EFs [49,84]. MoSSe/BP does not show NFEG states, while the response of the conduction band edge in InSe/BP masks the NFEG states. Clearly, the electronic structure and electrostatic potential in Na_2Te/Cs_2S are different, where under the action of both positive and negative EFs, the NFEG states descend to the Fermi level and the valence band edge to close the band gap.

(b) Electrostatic potential. As the external EF contributes a linear potential, it is important to study the variation in the electrostatic potential in the heterostructure with applied EF. Figure S14 in the SM [51] depicts the changes in the electrostatic potential with applied EF of varying strengths.

Since the vacuum thickness has been shown to play a role in the closure of band gap via the application of an EF [30], vacuum thicknesses of 25 and 50 Å have been employed in this paper.

For a fixed vacuum thickness, the spatial extent of the linear potential contributed by the external EF decreases, while the slope of this linear potential is found to increase with the magnitude of the applied EF, as shown by Fig. 8. Again, upon increasing the vacuum thickness for a fixed EF, the spatial extent of the linear potential is only found to increase, as evident from Fig. 9. The change in the linear potential induces the observed spatial shift in the NFEG states (marked in Fig. S16 in the SM [51]) with vacuum thickness and applied EF, as shown in Fig. S15 in the SM [51], consistent with Figs. 8 and 9. The NFEG states are also found to shift down in energy with increased vacuum thickness. Then increasing the vacuum thickness is found to lower the EF required to close the band gap, as shown in Fig. S16 in the SM [51], which conforms to an earlier finding by Zhou *et al.* [30]. Moreover, to check the sensitivity of results to the vacuum thickness, the unrelaxed and relaxed structures at 50 Å vacuum thickness are compared systematically with that of 25 Å vacuum thickness, as shown in Fig. S17 in the SM [51]. In conformance with an earlier study [30], a higher vacuum thickness is found to close the band gap at a smaller EF. As shown in Fig. S17 in the SM [51], the EF needed to close the band gap drops down appreciably upon increasing the vacuum thickness. Further, relaxation is not found to cause a major change in the band structure and the EF required to close the band gap, which is like the earlier observations noted at 25 Å vacuum thickness, as projected in Fig. S17 in the SM [51]. At 50 Å vacuum thickness, the band gap is closed at -0.21 (-0.23) V/Å and 0.19 (0.225) V/Å of positive and negative EFs, respectively, in the unrelaxed (relaxed) structures, while with 25 Å vacuum thickness, the band gap closed at -0.33 (-0.33) V/Å and 0.31 (0.34) V/Å for positive and negative EFs, respectively, in unrelaxed (relaxed) structures. Interestingly, the interlayer relaxation reduces drastically to a negligible level upon raising the vacuum thickness to 50 Å. Interlayer relaxation of 0.48 and 0.02 Å noticed at 25 Å vacuum thickness (under the application of positive and negative applied EFs, respectively) drops to 0.09 and 0.01 Å at 50 Å vacuum thickness. Table S3 in the SM [51] lists the bond lengths and interlayer distances for both unrelaxed and relaxed structures at the two vacuum thicknesses.

As noted in the preceding subsections, the same trend is shown by both positive and negative EFs. Likewise, the electrostatic potential exhibits a similar pattern with a positive EF, which is shown in Fig. S14 in the SM [51].

(c) Electrical conductivity. As most electronic devices are integrated with gate voltage, the population/density of charge carriers in the system can be controllably moderated via gating. The increased population/density of carriers can enhance the response in terms of electrical current or conductivity immensely in the system. The study on MX_2 (TMDC) monolayers has shown a large effect of the EF on transport properties of the monolayers [94]. Thus, with the NFEG bands in the Na_2Te/Cs_2S heterostructure, it is expected to have a significant improvement in the electrical conductivity. In Fig. 10, the variation of electrical conductivity with the EF along the positive and negative z direction has been shown where the negative (yellow) and positive (green) $\mu = (E - E_F)$ represent the p- and n-type regions of the vdWH.

The electrical conductivities in p- and n-type regions show different EF responses, which is consistent with the faster movement of the conduction bands toward the Fermi level than that of the valence bands, as noted in Fig. 7. The electrical

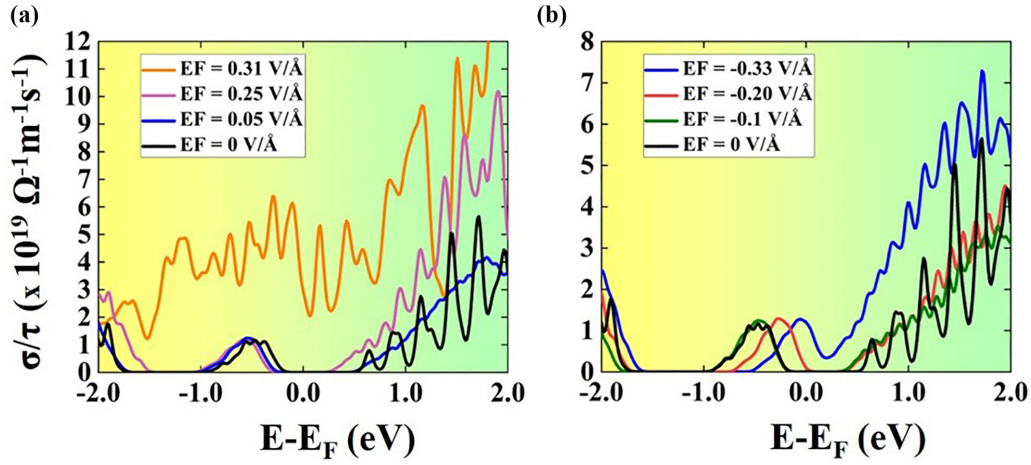

FIG. 10. Change in electrical conductivity of Na_2Te/Cs_2S heterostructure with applied electric field (along both directions) at the temperature $T = 300$ K. The right (green) region for $E-E_F > 0$ represents n-type conductivity, and the left (yellow) region corresponding to $E-E_F < 0$ represents p-type conductivity.

conductivity is not very enhanced near the valence band by increasing the EF along any direction, while for the near conduction band region (i.e., for positive chemical potential), conductivity drops at first under a small EF. This fall in the electrical conductivity has resulted from the increased collisional effect or scattering phenomena upon the introduction of EF [95]. However, as the EF increases and the heterostructure reaches toward the metallization, the conductivity shows a sharp boost. The increment in the electrical conductivity is clearly reflected from the increased electronic DOS observed in Fig. S18 in the SM [51]. From the DOS plot, it is observed that the charge density increases immensely at the EF of 0.31 V/Å and thereby results in an enhanced electrical conductivity of the heterostructure. This overlays the way for the development of the Na_2Te/Cs_2S heterostructure-based nanoelectronic devices for futuristic applications.

IV. CONCLUSIONS

Ab initio investigations on the electronic, mechanical, and the piezotronic properties of the family of 2D dialkali metal monochalcogenide M_2X monolayers have been carried out systematically, which reveal a semiconducting band gap in the monolayers and low piezoelectric strain coefficients $d_{33} \sim -0.5$ to $+2.0$ pm V^{-1} along with extreme flexibility, attested by small Young's modulus $Y \sim 50$ to 8 N m^{-1}. The heterostructures formed from the family of monolayers have led to significant improvement in the negative out-of-plane piezoelectricity with the highest longitudinal negative piezoelectric coefficient $d_{33} = -39$ pm V^{-1} found in the Na_2Te/Cs_2S heterostructure. The rise in the piezoelectric coefficient d_{33} in this specific heterostructure has been seen to appear due to the large band offset of ~ 0.6–1.4 eV and electrostatic potential energy difference among the layers. The out-of-plane dipole moment that builds up in the heterostructure is -0.008 D. The anomalous nature of the negative piezoelectric property owes its origin to the very small out-of-plane elastic stiffness and Young's modulus, which is brought up by the weak vdW interlayer interactions. It is analogous to the layered structure of $CuInP_2S_6$ investigated earlier. The soft interactions at the interface have been affirmed by the small out-of-plane Young's modulus ($Y \sim 11$ N m^{-1}). The small in-plane ($Y \sim 22$ N m^{-1}) and out-of-plane ($Y \sim 11$ N m^{-1}) flexibilities mark the heterostructure as a superior material for flexible electronics devices. The prominent response to the external stimuli, i.e., the vertical strain and EF, is observed to modulate the electronic properties of the heterostructure. The vertical compressive strain causes the band gap enlarging, while vertical EF induces the gradual narrowing and closure of the band gap, bringing the semiconducting-to-metallic transition at a low EF of 0.31 and -0.33 V/Å. The latter results in a high DOS close to the Fermi level as the result of shifting of the NFEG bands and conduction band edge moving to the Fermi level. The presence of these high density of surface states near the Fermi level largely boosts the charge carrier transport and electrical conductivity. Low-power-consumption data storage devices can be envisioned based on the proposed vdWH, where the device can be turned from OFF to ON state and vice versa via small gate voltage. Moreover, the highly negative piezoelectric properties together with perturbation-induced tunability in electrical conductivity can be effectively utilized in piezotronics devices and next-generation electronic devices.

ACKNOWLEDGMENTS

A.A. acknowledges the Council of Scientific & and Industrial Research fellowship, while A.R. thanks INST-Mohali, India, for the fellowship.The supercomputing resources provided by INST, Mohali, PARAM YUVA II of CDAC, Pune, and PARAM-SHIVAY at IIT, Varanasi, under the National Supercomputing Mission, Government of India, are greatly saluted.

[1] K. S. Novoselov, A. K. Geim, S. V. Morozov, D. Jiang, Y. Zhang, S. V. Dubonos, I. V. Grigorieva, and A. A. Firsov, Electric field effect in atomically thin carbon films, Science **306**, 666 (2004).

[2] G. Fiori, F. Bonaccorso, G. Iannaccone, T. Palacios, D. Neumaier, A. Seabaugh, S. K. Banerjee, and L. Colombo, Electronics based on two-dimensional materials, Nat. Nanotechnol. **9**, 768 (2014).

[3] R. Fei, W. Li, J. Li, and L. Yang, Giant piezoelectricity of monolayer group IV monochalcogenides: SnSe, SnS, GeSe, and GeS, Appl. Phys. Lett. **107**, 173104 (2015).

[4] F. Li, T. Shen, C. Wang, Y. Zhang, J. Qi, and H. Zhang, Recent advances in strain-induced piezoelectric and piezoresistive effect-engineered 2D semiconductors for adaptive electronics and optoelectronics, Nano Lett. **12**, 106 (2020).

[5] R. Hinchet, U. Khan, C. Falconi, and S. W. Kim, Piezoelectric properties in two-dimensional materials: Simulations and experiments, Mater. Today **21**, 611 (2018).

[6] H. Wang, K. Kurata, T. Fukunaga, H. Ago, H. Takamatsu, X. Zhang, T. Ikuta, K. Takahashi, T. Nishiyama, and Y. Takata, Simultaneous measurement of electrical and thermal conductivities of suspended monolayer graphene, J. Appl. Phys. **119**, 244306 (2016).

[7] H. Li, Q. Zhang, C. C. R. Yap, B. K. Tay, T. H. T. Edwin, A. Olivier, and D. Baillargeat, From bulk to monolayer MoS_2: Evolution of Raman scattering, Adv. Funct. Mater. **22**, 1385 (2012).

[8] M. Akhtar, G. Anderson, R. Zhao, A. Alruqi, J. E. Mroczkowska, G. Sumanasekera, and J. B. Jasinski, Recent advances in synthesis, properties, and applications of phosphorene, npj 2D Mater. Appl. **1**, 5 (2017).

[9] J. Dai and X. C. Zeng, Titanium trisulfide monolayer: Theoretical prediction of a new direct-gap semiconductor with high and anisotropic carrier mobility, Angew. Chem. Int. Ed. **54**, 7572 (2015).

[10] K. F. Mak, C. Lee, J. Hone, J. Shan, and T. F. Heinz, Atomically Thin MoS_2: A New Direct-Gap Semiconductor, Phys. Rev. Lett. **105**, 136805 (2010).

[11] C. Lei, Y. Ma, X. Xu, T. Zhang, B. Huang, and Y. Dai, Broken-gap type-III band alignment in WTe_2/HfS_2 van der Waals heterostructure, J. Phys. Chem. C **123**, 23089 (2019).

[12] H. Zhang, Y. N. Zhang, H. Liu, and L. M. Liu, Novel heterostructures by stacking layered molybdenum disulfides and nitrides for solar energy conversion, J. Mater. Chem. A Mater. **2**, 15389 (2014).

[13] M. Y. Li, C. H. Chen, Y. Shi, and L. J. Li, Heterostructures based on two-dimensional layered materials and their potential applications, Mater. Today **19**, 322 (2016).

[14] M. K. Mohanta, A. Arora, and A. D. Sarkar, Conflux of tunable Rashba effect and piezoelectricity in flexible magnesium monochalcogenide monolayers for next-generation spintronic devices, Nanoscale **13**, 8210 (2021).

[15] S. Yuan, W. F. Io, J. Mao, Y. Chen, X. Luo, and J. Hao, Enhanced piezoelectric response of layered In_2Se_3/MoS_2 nanosheet-based van der Waals heterostructures, ACS Appl. Nano Mater. **3**, 11979 (2020).

[16] K. A. N. Duerloo, M. T. Ong, and E. J. Reed, Intrinsic piezoelectricity in two-dimensional materials, J. Phys. Chem. Lett. **3**, 2871 (2012).

[17] J. Shi, C. Han, X. Wang, and S. Yun, Electronic, elastic and piezoelectric properties of boron-V group binary and ternary monolayers, Phys. B: Condens. Matter **574**, 311634 (2019).

[18] S. Yu, Q. Rice, B. Tabibi, Q. Li, and F. J. Seo, Piezoelectricity in WSe_2 /MoS_2 heterostructure atomic layers, Nanoscale **10**, 12472 (2018).

[19] M. K. Mohanta, A. Rawat, N. Jena Dimple, R. Ahammed, and A. D. Sarkar, Superhigh out-of-plane piezoelectricity, low thermal conductivity and photocatalytic abilities in ultrathin 2D van der Waals heterostructures of boron monophosphide and gallium nitride, Nanoscale **11**, 21880 (2019).

[20] L. Dong, J. Lou, and V. B. Shenoy, Large in-plane and vertical piezoelectricity in Janus transition metal dichalchogenides, ACS Nano **11**, 8242 (2017).

[21] P. Nandi, A. Rawat, R. Ahammed, N. Jena, and A. D. Sarkar, Group-IV(A) Janus dichalcogenide monolayers and their interfaces straddle gigantic shear and in-plane piezoelectricity, Nanoscale **13**, 5460 (2021).

[22] I. Katsouras, K. Asadi, M. Li, T. B. van Driel, K. S. Kjær, D. Zhao, T. Lenz, Y. Gu, P. W. M. Blom, D. Damjanovic *et al.*, The negative piezoelectric effect of the ferroelectric polymer poly(vinylidene fluoride), Nat. Mater. **15**, 78 (2016).

[23] L. You, Y. Zhang, S. Zhou, A. Chaturvedi, S. A. Morris, F. Liu, L. Chang, D. Ichinose, and H. Funakubo, Origin of giant negative piezoelectricity in a layered van der Waals ferroelectric, Sci. Adv. **5**, 3780 (2019).

[24] J. Kim, K. M. Rabe, and D. Vanderbilt, Negative piezoelectric response of van der Waals layered bismuth tellurohalides, Phys. Rev. B **100**, 104115 (2019).

[25] C. v. Nguyen and N. N. Hieu, Effect of biaxial strain and external electric field on electronic properties of MoS_2 monolayer: A first-principle study, Chem. Phys. **468**, 9 (2016).

[26] B. S. Kim, W. S. Kyung, J. J. Seo, J. Y. Kwon, J. D. Denlinger, C. Kim, and S. R. Park, Possible electric field induced indirect to direct band gap transition in $MoSe_2$, Sci. Rep. **7**, 5206 (2017).

[27] D. Singh, S. K. Gupta, I. Lukačević, M. Mužević, Y. Sonvane, and R. Ahuja, Effect of electric field on optoelectronic properties of indiene monolayer for photoelectric nanodevices, Sci. Rep. **9**, 17300 (2019).

[28] R. Chegel and S. Behzad, Tunable electronic, optical, and thermal properties of two- dimensional germanene via an external electric field, Sci. Rep. **10**, 704 (2020).

[29] M. Khazaei, A. Ranjbar, M. Ghorbani-Asl, M. Arai, T. Sasaki, Y. Liang, and S. Yunoki, Nearly free electron states in MXenes, Phys. Rev. B **93**, 205125 (2016).

[30] J. Zhou, M. Khazaei, A. Ranjbar, V. Wang, T. D. Kühne, K. Ohno, Y. Kawazoe, and Y. Liang, Modulation of nearly free electron states in hydroxyl-functionalized MXenes: A first-principles study, J. Mater. Chem. C Mater. **8**, 5211 (2020).

[31] X. Yang, B. Sa, H. Zhan, and Z. Sun, Electric field-modulated data storage in bilayer InSe, J. Mater. Chem. C Mater. **5**, 12228 (2017).

[32] S. Zhao, Z. Li, and J. Yang, Obtaining two-dimensional electron gas in free space without resorting to electron doping: An electride based design, J. Am. Chem. Soc. **136**, 13313 (2014).

[33] G. Kresse and J. Furthmüller, Efficient iterative schemes for *ab initio* total-energy calculations using a plane-wave basis set, Phys. Rev. B **54**, 11169 (1996).

[34] G. Kresse and J. Hafner, *Ab initio* molecular dynamics for liquid metals, Phys. Rev. B **47**, 558 (1993).

[35] G. Kresse and J. Hafner, *Ab initio* molecular-dynamics simulation of the liquid-metal–amorphous-semiconductor transition in germanium, Phys. Rev. B **49**, 14251 (1994).

[36] G. Kresse and J. Furthmüller, Efficiency of *ab-initio* total energy calculations for metals and semiconductors using a plane-wave basis set, Comput. Mater. Sci. **6**, 15 (1996).

[37] P. E. Blöchl, Projector augmented-wave method, Phys. Rev. B **50**, 17953 (1994).

[38] J. P. Perdew, K. Burke, and M. Ernzerhof, Generalized Gradient Approximation Made Simple, Phys. Rev. Lett. **77**, 3865 (1996).

[39] J. P. Perdew, K. Burke, and M. Ernzerhof, Generalized Gradient Approximation Made Simple [Phys. Rev. Lett. 77, 3865 (1996)], Phys. Rev. Lett. **78**, 1396 (1997).

[40] J. Heyd, G. E. Scuseria, and M. Ernzerhof, Hybrid functionals based on a screened Coulomb potential, J. Chem. Phys. **118**, 8207 (2003).

[41] A. V. Krukau, O. A. Vydrov, A. F. Izmaylov, and G. E. Scuseria, Influence of the exchange screening parameter on the performance of screened hybrid functionals, J. Chem. Phys. **125**, 224106 (2006).

[42] S. Grimme, J. Antony, S. Ehrlich, and H. Krieg, A consistent and accurate *ab initio* parametrization of density functional dispersion correction (DFT-D) for the 94 elements H-Pu, J. Chem. Phys. **132**, 154104 (2010).

[43] S. Grimme, S. Ehrlich, and L. Goerigk, Effect of the damping function in dispersion corrected density functional theory, J. Comput. Chem. **32**, 1456 (2011).

[44] G. K. H. Madsen, J. Carrete, and M. J. Verstraete, BOLTZTRAP2, a program for interpolating band structures and calculating semi-classical transport coefficients, Comput. Phys. Commun. **231**, 140 (2017).

[45] C. Freysoldt, A. Mishra, M. Ashton, and J. Neugebauer, Generalized dipole correction for charged surfaces in the repeated-slab approach, Phys. Rev. B **102**, 045403 (2020).

[46] J. Neugebauer and M. Scheffler, Adsorbate-substrate and adsorbate-adsorbate interactions of Na and K adlayers on Al(111), Phys. Rev. B **46**, 16067 (1992).

[47] X.-P. Wang, X.-B. Li, N.-K. Chen, J.-H. Zhao, Q.-D. Chen, and H.-B. Sun, Electric field analyses on monolayer semiconductors: The example of InSe, Phys. Chem. Chem. Phys. **20**, 6945 (2018).

[48] M. K. Mohanta, A. Arora, and A. D. Sarkar, Effective modulation of ohmic contact and carrier concentration in a graphene-MgX (X = S, Se) van der Waals heterojunction with tunable band-gap opening via strain and electric field, Phys. Rev. B **104**, 165421 (2021).

[49] M. K. Mohanta, A. Kishore, and A. D. Sarkar, Two-dimensional ultrathin van der Waals heterostructures of indium selenide and boron monophosphide for superfast nanoelectronics, excitonic solar cells, and digital data storage devices, Nanotechnology **31**, 15 (2020).

[50] B. Ghosh, S. Nahas, S. Bhowmick, and A. Agarwal, Electric field induced gap modification in ultrathin blue phosphorus, Phys. Rev. B **91**, 115433 (2015).

[51] See Supplemental Material at http://link.aps.org/supplemental/10.1103/PhysRevB.107.085402 for electronic spectra, phonon spectra, Young's modulus, Poisson's ratio, out-of-plane piezoelectricity, interfacial properties, structural parameter in the EF, work function, and dipole with interlayer distance.

[52] C. Hua, F. Sheng, Q. Hu, Z. A. Xu, Y. Lu, and Y. Zheng, Dialkali-metal monochalcogenide semiconductors with high mobility and tunable magnetism, J. Phys. Chem. Lett. **9**, 6695 (2018).

[53] A. Rawat, A. Arora, and A. D. Sarkar, Interfacing 2D M_2X (M = Na, K, Cs; X = O, S, Se, Te) monolayers for 2D excitonic and tandem solar cells, Appl. Surf. Sci. **563**, 150304 (2021).

[54] S. Radescu, D. Machon, and P. Mélinon, Origin of dynamical instabilities in some simulated 2D materials: GaSe as a case study, Phys. Rev. Mater. **3**, 074002 (2019).

[55] V. Zólyomi, N. D. Drummond, and V. I. Fal'ko, Electrons and phonons in single layers of hexagonal indium chalcogenides from *ab initio* calculations, Phys. Rev. B **89**, 205416 (2014).

[56] F. Mouhat and F.-X. Coudert, Necessary and sufficient elastic stability conditions in various crystal systems, Phys. Rev. B **90**, 224104 (2014).

[57] G. Cao, Atomistic studies of mechanical properties of graphene, Polymers (Basel) **6**, 2404 (2014).

[58] R. C. Cooper, C. Lee, C. A. Marianetti, X. Wei, J. Hone, and J. W. Kysar, Nonlinear elastic behavior of two-dimensional molybdenum disulfide, Phys. Rev. B **87**, 035423 (2013).

[59] F. Zeng, W. B. Zhang, and B. Y. Tang, Electronic structures and elastic properties of monolayer and bilayer transition metal dichalcogenides MX_2 (M = Mo, W; X = O, S, Se, Te): A comparative first-principles study, Chin. Phys. B **24**, 097103 (2015).

[60] R. C. Andrew, R. E. Mapasha, A. M. Ukpong, and N. Chetty, Mechanical properties of graphene and boronitrene, Phys. Rev. B **85**, 125428 (2012).

[61] H. Zhang and R. Wang, The stability and the nonlinear elasticity of 2D hexagonal structures of Si and Ge from first-principles calculations, Phys. B: Condens. Matter **406**, 4080 (2011).

[62] E. Cadelano, P. L. Palla, S. Giordano, and L. Colombo, Elastic properties of hydrogenated graphene, Phys. Rev. B **82**, 235414 (2010).

[63] T. N. Do, N. N. Hieu, N. A. Poklonski, N. T. Thanh Binh, C. Q. Nguyen, and N. D. Hien, Computational insights into structural, electronic, and optical properties of Janus GeSO monolayer, RSC. Adv. **11**, 28381 (2021).

[64] M. de Jong, W. Chen, H. Geerlings, M. Asta, and K. A. Persson, A database to enable discovery and design of piezoelectric materials, Sci. Data **2**, 150053 (2015).

[65] M. N. Blonsky, H. L. Zhuang, A. K. Singh, and R. G. Hennig, *Ab initio* prediction of piezoelectricity in two-dimensional materials, ACS Nano **9**, 9885 (2015).

[66] J. Kang, S. Tongay, J. Zhou, J. Li, and J. Wu, Band offsets and heterostructures of two-dimensional semiconductors, Appl. Phys. Lett. **102**, 012111 (2013).

[67] L. Hu and X. Huang, Peculiar electronic, strong in-plane and out-of-plane second harmonic generation and piezoelectric properties of atom-thick α-M_2X_3 (M = Ga, In; X = S, Se): Role of spontaneous electric dipole orientations, RSC Adv. **7**, 55034 (2017).

[68] K. Liu, Q. Yan, M. Chen, W. Fan, Y. Sun, J. Suh, D. Fu, S. Lee, J. Zhou, S. Tongay, J. Ji, J. B. Neaton, and J. Wu, Elastic properties of chemical-vapor-deposited monolayer MoS_2, WS_2, and their bilayer heterostructures, Nano Lett. **14**, 5097 (2014).

[69] J. H. Lee, J. Y. Park, E. B. Cho, T. Y. Kim, S. A. Han, T. H. Kim, Y. Liu, S. K. Kim, C. J. Roh, H. J. Yoon *et al.*, Reliable

piezoelectricity in bilayer Wse_2 for piezoelectric nanogenerators, Adv. Mater. **29**, 1606667 (2017).

[70] Q. Peng, K. Hu, B. Sa, J. Zhou, B. Wu, X. Hou, and Z. Sun, Unexpected elastic isotropy in a black phosphorene/TiC_2 van der Waals heterostructure with flexible Li-ion battery anode applications, Nano Res. **10**, 3136 (2017).

[71] Z. Guo, N. Miao, J. Zhou, B. Sa, and Z. Sun, Strain-mediated type-I/type-II transition in Mxene/blue phosphorene van der Waals heterostructures for flexible optical/electronic devices, J. Mater. Chem. C **5**, 978 (2017).

[72] A. Samad, M. Noor-A-Alam, and Y.-H. Shin, First principles study of a SnS_2/graphene heterostructure: A promising anode material for rechargeable Na ion batteries, J. Mater. Chem. A **4**, 14316 (2016).

[73] J. Liu, Y. Liu, Y. Yang, X. Bai, L. Liu, K. Yang, H. Ali, Y. Zhao, B. Wu, B. Sa *et al.*, GeP_3/NbX_2 (X = S, Se) nano-heterostructures: promising isotropic flexible anodes for lithium-ion batteries with high lithium storage capacity, ACS Omega **6**, 2956 (2021).

[74] N. Ghobadi, Normal compressive strain-induced modulation of electronic and mechanical properties of multilayer MoS_2 and graphene/MoS_2 heterostructure: A first-principles study, Physica E **111**, 158 (2019).

[75] R. Ahammed, N. Jena, A. Rawat, M. K. Mohanta, and A. de Sarkar, Ultrahigh out-of-plane piezoelectricity meets giant Rashba effect in 2D Janus monolayers and bilayers of group IV transition-metal trichalcogenides, J. Phys. Chem. C **124**, 21250 (2020).

[76] T. Zhang, Y. Liang, H. Guo, H. Fan, and X. Tian, The high piezoelectricity, flexibility and electronic properties of new Janus $ZnXY_2$ (X = Ge, Sn, Si and Y = S, Se, Te) monolayers: A first-principles research, Appl. Surf. Sci. **579**, 152017 (2022).

[77] M. K. Mohanta, F. Is, A. Kishore, and A. De Sarkar, Spin-current modulation in hexagonal buckled ZnTe and CdTe monolayers for self-powered flexible-piezo-spintronic devices, ACS Appl. Mater. Interfaces **13**, 40872 (2021).

[78] M. K. Mohanta and A. De Sarkar, Coupled spin and valley polarization in monolayer HfN_2 and valley-contrasting physics at the HfN_2-Wse_2 interface, Phys. Rev. B **102**, 125414 (2020).

[79] G. Casillas, U. Santiago, H. BarroÌn, D. Alducin, A. Ponce, and M. José-Yacamán, Elasticity of MoS_2 sheets by mechanical deformation observed by *in situ* electron microscopy, J. Phys. Chem. C **119**, 710 (2015).

[80] R. Li, Q. Shao, E. Gao, and Z. Liu, Elastic anisotropy measure for two-dimensional crystals, Extreme Mech. Lett. **34**, 100615 (2020).

[81] Y. Liu, H. Xiao, and W. A. Goddard, Schottky-barrier-free contacts with two-dimensional semiconductors by surface-engineered Mxenes, J. Am. Chem. Soc. **138**, 15853 (2016).

[82] X. H. Li, B. J. Wang, G. D. Wang, X. F. Yang, R. Q. Zhao, X. T. Jia, and S. H. Ke, A two-dimensional arsenene/g-C_3N_4 van der Waals heterostructure: A highly efficient photocatalyst for water splitting, Sustain Energy Fuels **5**, 2249 (2021).

[83] P. C. Sherrell, M. Fronzi, N. A. Shepelin, A. Corletto, D. A. Winkler, M. Ford, J. G. Shapter, and A. V. Ellis, A bright future for engineering piezoelectric 2D crystals, Chem. Soc. Rev. **51**, 650 (2022).

[84] M. K. Mohanta and A. D. Sarkar, Interfacial hybridization of Janus MoSSe and BX (X = P, As) monolayers for ultrathin excitonic solar cells, nanopiezotronics and low-power memory devices, Nanoscale **12**, 22645 (2020).

[85] Z. Peng, X. Chen, Y. Fan, D. J. Srolovitz, and D. Lei, Strain engineering of 2D semiconductors and graphene: from strain fields to band-structure tuning and photonic applications, Light Sci. Appl. **9**, 190 (2020).

[86] Y. Bai, Strain effects on the energy band structure and electronic states of single-layer $MoTe_2$, Wte_2 and their heterostructures, Integr. Ferroelectr. **182**, 30 (2017).

[87] Z. Guan, C. S. Lian, S. Hu, S. Ni, J. Li, and W. Duan, Tunable structural, electronic, and optical properties of layered two-dimensional C_2N and MoS_2 van der Waals heterostructure as photovoltaic material, J. Phys. Chem. C **121**, 3654 (2017).

[88] Z. Guan, S. Ni, and S. Hu, Band gap opening of graphene by forming a graphene/$PtSe_2$ van der Waals heterojunction, RSC Adv. **7**, 45393 (2017).

[89] Y. Sun, D. Wang, and Z. Shuai, Indirect-to-direct band gap crossover in few-layer transition metal dichalcogenides: A theoretical prediction, J. Phys. Chem. C **120**, 21866 (2016).

[90] H. T. T. Nguyen, V. v. Tuan, C. v. Nguyen, H. v. Phuc, H. D. Tong, S. T. Nguyen, and N. N. Hieu, Electronic and optical properties of a Janus SnSSe monolayer: Effects of strain and electric field, Phys. Chem. Chem. Phys. **22**, 11637 (2020).

[91] M. Luo, Y. E. Xu, and Q. X. Zhang, Modulation of band gap by an applied electric field in BN-based heterostructures, Solid State Commun. **273**, 44 (2018).

[92] S. Kaur, A. Kumar, S. Srivastava, and K. Tankeshwar, van der Waals heterostructures based on allotropes of phosphorene and $MoSe_2$, Phys. Chem. Chem. Phys. **19**, 22023 (2017).

[93] M. K. Mohanta, H. Seksaria, and A. D. Sarkar, Insights into CrS_2 monolayer and n-CrS_2/p-HfN_2 interface for low-power digital and analog nanoelectronics, Appl. Surf. Sci. **579**, 152211 (2022).

[94] M. Li, E. W. Du, Y. Y. Liang, Y. H. Shen, J. Chen, W. Ju, Y. An, and S. J. Gong, Electric control of nearly free electron states and ferromagnetism in the transition-metal dichalcogenides monolayers, J. Phys. Condens. Matter **33**, 205702 (2021).

[95] R. Chegel, Enhanced electrical conductivity in graphene and boron nitride nanoribbons in large electric fields, Phys. B: Condens. Matter **531**, 206 (2018).

[96] M. Otani and S. Okada, Field-induced free-electron carriers in graphite, J. Phys. Soc. Jpn. **79**, 073701 (2010).

[97] X. Cui, D. Han, H. Guo, L. Zhou, J. Qiao, Q. Liu, Z. Cui, and C. Lin Y.Li, Realizing nearly-free-electron like conduction band in a molecular film through mediating intermolecular van der Waals interactions, Nat. Commun. **10**, 3374 (2019).

[98] L. Kong, L. Liu, L. Chen, Q. Zhong, P. Cheng, H. Li, Z. Zhang, and K. Wu, One-dimensional nearly free electron states in borophene, Nanoscale **11**, 15605 (2019).

[99] M. Shibuta, K. Yamamoto, H. Guo, J. Zhao, and A. Nakajima, Highly dispersive nearly free electron bands at a 2D-assembled C_{60} monolayer, J. Phys. Chem. C **124**, 734 (2020).